High-Performance Composite Electrolytes for Solid-State Lithium Metal Batteries: Enhancing Ionic Conductivity and Interfacial Compatibility through Polyvinylpyrrolidone Blending and Inorganic Filler Incorporation

Pratiksha Gami and Sunil Kumar*

Department of Metallurgical Engineering and Materials Science, Indian Institute of Technology Indore, Simrol, 453552, India.

*Corresponding author, E-mail: sunil@iiti.ac.in

Phone No.: (+91)-731660-3281

Abstract:

One of the significant challenges in advancing safe and high-energy-density solid-state lithium metal batteries is achieving high ionic conductivities and ensuring good interfacial compatibility between the solid electrolyte and the electrodes. To address these challenges, the study proposes a composite electrolyte that is made through a solution casting method, utilizing polyvinylidene fluoride hexafluorophosphate (PVDF-HFP) and polyvinylpyrrolidone (PVP) in conjunction with lithium bis(trifluoromethanesulfonyl)imide (LiTFSI) salt and mid-entropy inorganic filler $Li_{1.5}Sn_{1.0}Al_{0.5}Zr_{0.5}(PO_4)_3$. The polymer blend with an optimized ceramic filler exhibits an exceptional room-temperature ionic conductivity 1.48×10^{-4} S cm^{-1}, a significantly high Li-ion transference number of 0.74, and shows electrochemical stability up to 4.58 V. The symmetric Li||Li cell fabricated with the composite electrolyte exhibits uniform Li^+ deposition/stripping for over >500 h at 2 mA cm^{-2}. Further, a full cell with $LiFePO_4$ cathode and lithium anode is fabricated and shows excellent electrochemical performance with 78% capacity retention after 1000 cycles at 2C. The findings from this study advance the development of practical inorganic polymer electrolytes for fast-charging lithium batteries.

Keywords: Inorganic Polymer Electrolytes, Fast-charging Lithium Metal Batteries, Ionic Conductivity, Lithium-ion Transference Number, GCD.

1. Introduction

The global shift toward carbon-neutral initiatives has accelerated the demand for advanced energy storage solutions, driving innovations in battery technology [1, 2]. Conventional lithium batteries, the present workhorse in the energy sector, while ubiquitous, are increasingly constrained in their ability to meet the heightened requirements for energy density, rapid charging, and safety in emerging markets [3, 4]. Lithium-metal batteries (LMBs) featuring lithium-metal anodes have emerged as a compelling substitute due to their exceptional theoretical specific capacity (3860 mAh g^{-1}), low redox potential (-3.04 V *vs.* SHE), and lightweight characteristics [5-7]. However, LMBs confront considerable hurdles, notably with traditional carbonate-based liquid electrolytes, which have incompatibility with Li, poor Coulombic efficiency, combustibility, and a propensity for dendrite formation at high current densities [8-10]. These limitations highlight the pressing need for alternative electrolytes capable of delivering ultra-fast charging, enhanced safety, and stable cycling performance [11].

Composite electrolytes (CEs) have garnered significant attention as a promising solution, offering the advantages of high ionic conductivity, non-flammability, and superior thermal and electrochemical stability [12-15]. By combining the favorable characteristics of inorganic electrolytes with the flexibility and processability of polymer matrices, CEs address the challenges traditional electrolytes face in LMBs [16-20]. Recent developments in CEs have explored various material systems, including lithium salts and additives such as succinonitrile, demonstrating improved cycling performance and thermal stability [21-23]. However, these systems often suffer from limitations such as high viscosity, low conductivity, and substantial polarization, which hinder their application in ultra-fast charging scenarios [22, 24, 25]. Fast-charging battery

technology aims to replenish up to 80% of fully discharged LMBs within 6-10 minutes, delivering a charging speed 5-7 times faster than conventional Li-ion batteries [26, 27].

Polyvinylpyrrolidone (PVP) has been utilized in lithium-metal batteries due to its unique molecular structural properties, moderate conductivity, good environmental stability, and favorable charge-transport behavior [28, 29]. The rigid pyrrolidone group in amorphous PVP enhances lithium-ion mobility. In contrast, the carbonyl group (CO) in its side chains forms complexes with various inorganic salts, contributing to stabilizing both electrodes at high voltages [30-32]. This feature helps batteries operate better over long-term cycling. Nevertheless, no earlier investigations have reported the employment of PVP and PVDF-HFP as polymer electrolytes (PE) in conjunction with lithium bis(trifluoromethane sulfonyl)imide (LiTFSI). In the current study, we discuss an exceptional composite electrolyte, referred to as IPE, composed of PE and mid-entropy $Li_{1.5}Sn_{1.0}Al_{0.5}Zr_{0.5}(PO_4)_3$ (LSAZP) inorganic filler in various weight fractions. This formulation leverages the combined strengths of its constituents: the polymer electrolyte provides flexibility and ion solvation, while the inorganic filler promotes Li^+ diffusion and stabilizes the electrode-electrolyte interface [33-36]. The enhanced ionic mobility and interface stability provided by this electrolyte system address the critical challenges associated with the fast charging of lithium-metal batteries [37-40]. These synergistic fusion yields improved Coulombic efficiency, enhanced safety due to low flammability, and an extended electrochemical stability range. From symmetric cell performance, it is clear that there is a stable interface between the electrolyte and Li metal. This work demonstrates the potential of the proposed inorganic polymer electrolyte as a pathway toward safer, more efficient, and higher-performance batteries for next-generation energy storage applications.

2. Results and Discussion:

The X-ray diffraction results for the PVP/PVDF-HFP/LiTFSI (PE) blend & inorganic filler LSAZP and IPE*x* (where *x* = 5, 10, 15, and 20 as the wt.% of filler) are shown in Figs. S1 and 1, respectively. Diffraction peaks at ~20° and 40° were noted for the polymer electrolyte [41]. Additionally, the introduction of LSAZP in the PE matrix results in the diffraction peaks (Figure 1) corresponding to the rhombohedral phase ($R\bar{3}c$ space group), matching the peaks of $Li_{1.5}Sn_{1.0}Al_{0.5}Zr_{0.5}(PO_4)_3$ [42]. The rhombohedral phase of LSAZP is more favorable for lithium-ion conduction compared to the amorphous phase of polymer, contributing to the stability of the composite material [43, 44]. Incorporating ceramic fillers decreases the relative intensity of the XRD peaks associated with PE, indicating reduced crystallinity in the polymer component of the electrolyte [12]. The diffraction peaks corresponding to the PE are discernable only in XRD patterns of IPE05 and IPE10. The increased LSAZP content intensifies the characteristic diffraction peaks associated with the inorganic filler. The IPE20 and LSAZP display very similar XRD patterns, indicating that even a 20 wt.% ceramic filler dominates the XRD pattern due to higher diffraction from the ceramic filler.

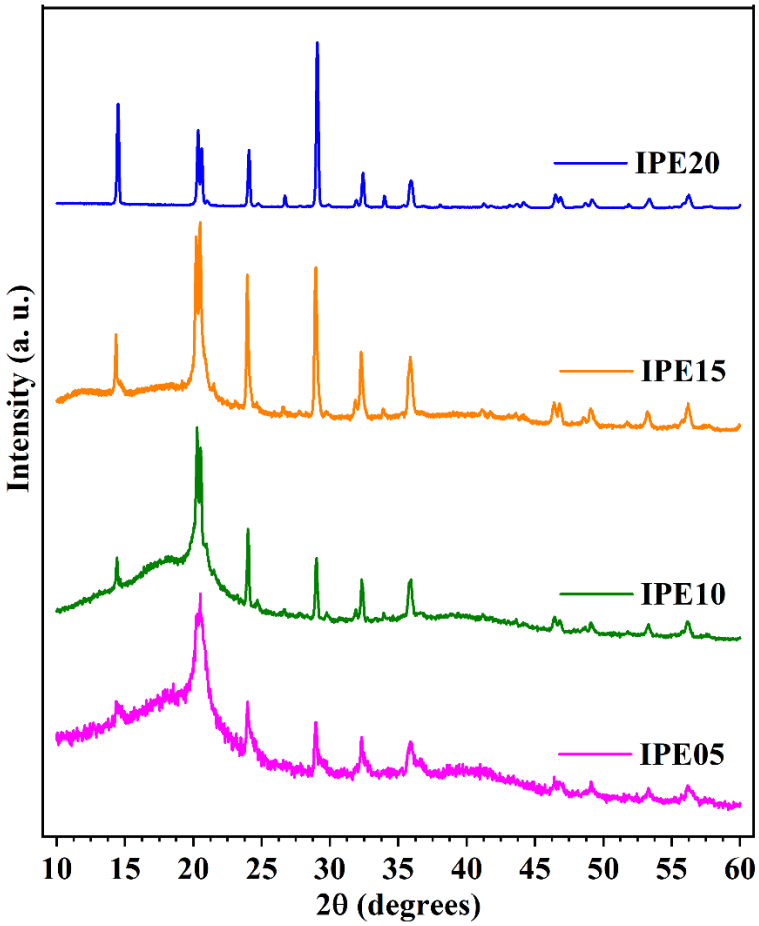

Fig. 1. XRD patterns of IPE05, IPE10, IPE15, and IPE20.

Fourier transform infrared (FTIR) spectroscopy was conducted to analyze the interactions in the electrolyte membranes. The FTIR spectra of the PE, LSAZP, and IPE*x* electrolyte films are shown in Figure S2. The peak at 625 cm^{-1} in the LSAZP ceramic's FTIR spectrum corresponds to the (Sn/Zr/Al-O6) octahedra's M-O bonds. The additional peaks in the spectrum are attributed to the P–O stretching vibration modes positioned at 560 and 943 cm^{-1}. The FTIR spectra of the PE and IPEx exhibit a broad band at 1655 cm^{-1}, which is associated with weak interactions such as H-bonding or electrostatic forces between polymer/polymer or polymer/ceramic entities [45]. A peak at 1353 cm^{-1} implies CH_2 wagging in the electrolyte [41].

The microstructures of composite electrolyte films are shown in Figs. 2 and S3. The random spheroid particles in the IPE15 film are LSAZP, and the surface of the PE sample (without LSAZP

filler) is smooth (Figs. S4(a) and S4(b)), and a similar structure was observed for the IPE05 (Figure S3(a)). Figure 2(b) presents the cross-sectional architecture of the IPE15 film, revealing a uniform thickness of ~60 μm, as further corroborated by Figure S5(i). Figs. S5(a-h) shows the element distribution mapping of Al, Zr, Sn, P, O, F, N, S, and C in the membrane. All elements are evenly distributed. In addition, Figure S6 shows a picture of a self-standing film.

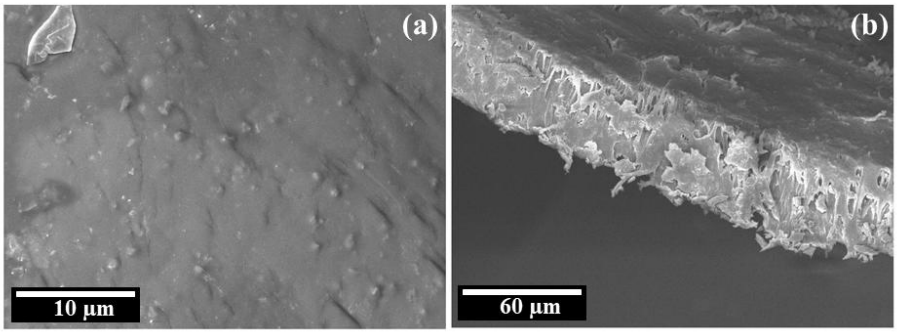

Fig. 2. SEM micrographs of (a) top surface and (b) cross-section of IPE15 film.

In composite electrolyte films, where both polymer and ceramics fillers serve as lithium-ion conducting media, the ion transport mechanism is highly complex due to the interplay between organic and inorganic lithium conductors. The lithium-ion conduction in the IPE*x* was evaluated through impedance spectroscopy with SS||IPE*x*||SS cell configuration. The resulting Nyquist plots exhibited semicircles in the high-frequency region, corresponding to the electrolyte resistance, along with an inclined tail in the low-frequency region, attributed to lithium-ion blocking effects (Figure 3(a)-(d)). Figure S7 displays the RT Nyquist plots of LSAZP and PE. The impedance data were deconvoluted with an equivalent circuit $(R_1||Q_1) + (Q_2)$ (Q stands for a constant-phase element, and R is a resistor). As the content of the inorganic filler increased, the intercept on the real axis progressively decreased, indicating a reduction in resistance up to the IPE15 membrane but rose again for IPE20. Table 1 shows the total ionic conductivity of all electrolyte membranes from the fitting process. The IPE15 has the highest $\sigma_{RT} = 1.48 \times 10^{-4}$ S cm^{-1}. However, further

increasing the inorganic filler in IPE20 leads to a decline in ionic conductivity, as the elevated LSAZP content basically hindered the passage of Li-ion [46]. The noticeable decrease was attributed to the agglomeration of these inorganic lithium-ion conductors particles, as the formation of agglomerated clusters decreased the volume ratio of the interface, thereby lessening the percolated network in the composite solid electrolyte [47]. Consequently, a significant portion of the bulk polymer phase cannot transform into a highly conductive interfacial phase, leading to a notable reduction in ionic conductivity at higher concentrations of LSAZP particles [48, 49]. Thus, it is anticipated that the ion transport mechanism in composite solid electrolytes is closely associated with the interfacial regions, where the polymer chains are influenced by the presence of inorganic fillers [50]. Figure S8 displays the ln σ vs. 1000/T plot for the CE15 film. The calculated activation energy (E_a) for Li^+ conduction was confirmed to ~ 0.33 eV using the linear fitting of the Arrhenius equation ($\sigma = \sigma_0 \exp(-E_a/k_BT)$; k_B is Boltzmann constant and σ_0 is pre-exponential factor). The low activation energy implies enhanced Li^+ ion mobility, indicating efficient ion transport pathways within the electrolyte membrane.

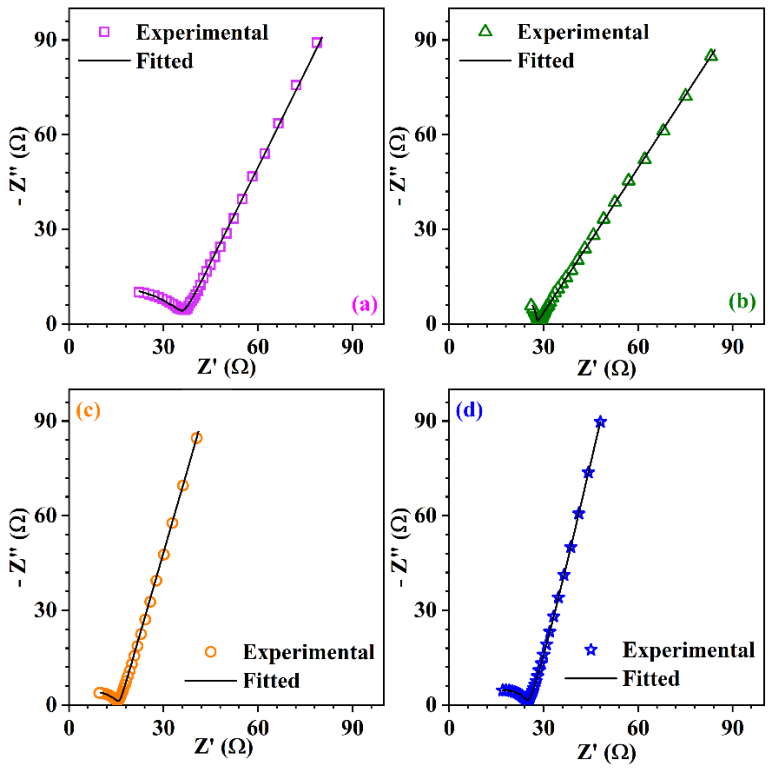

Fig. 3. RT Nyquist plots of (a) IPE05, (b) IPE10, (c) IPE15, and (d) IPE20. The impedance data is fitted with the equivalent circuit (R1||CPE1) + (CPE2).

Table 1. Total RT conductivity (σ_{RT}) of LSAZP, PE, and IPE*x* samples.

Sample	σ_{RT} **(S cm^{-1})**
LSAZP	2.95×10^{-4}
PE	2.84×10^{-5}
IPE05	6.47×10^{-5}
IPE10	8.23×10^{-5}
IPE15	1.48×10^{-4}

IPE20	9.24×10^{-5}

Thermal analysis plays a vital role in assessing the thermal stability of IPE15 under operational conditions. During cell operation, heat generation may lead to the degradation or melting of the solid electrolyte, potentially resulting in an internal short circuit. Therefore, ensuring the thermal stability of IPE15 is essential for the safe and reliable performance of the cell. The TGA curve of the IPE15 film, shown in Figure 4(a), the initial weight loss observed below 100 °C is likely due to the evaporation of residual or surface moisture [51]. The second weight loss stage, occurring between 345 °C and 485 °C, is attributed to the thermal degradation of the polymer backbone. The analysis shows that IPE15 remains thermally stable up to 345 °C, with only a 5 wt.% weight loss. This minor reduction suggests that the IPE films demonstrate good thermal stability. The free-standing polymer film exhibited excellent mechanical properties, as shown in Figure 4(b), where the mechanical performance was evaluated from 30 to 130 °C. At 30 °C, a high storage modulus >0.7 GPa was observed. When the temperature reached ~70 °C, a notable change in the storage modulus (E') was observed, attributed to the melting of the polymer's semicrystalline portion.

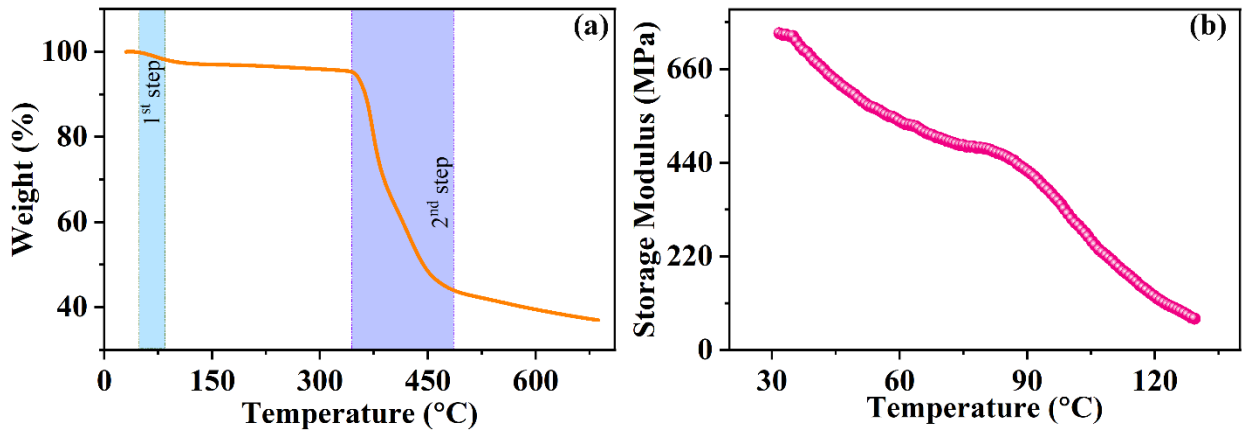

Fig. 4. (a) TGA plot and (b) DMA curve of IPE15.

One of the main challenges in achieving fast charging-discharging in LMBs is the development of a salt concentration gradient during operation. This occurs because the anion flux resulting from migration must be balanced by diffusion under steady-state conditions [52, 53]. To mitigate this, electrolytes with a higher fraction of cations available for migration, referred to as the cation transference number, are preferable [54]. The electrochemical performance of IPE15 was analyzed through chronoamperometry and Nyquist plots obtained before and after DC polarization (Figure 5(a)). These results revealed a stable Li^+ current of 34 µA after an initial decrease from 44 µA, demonstrating excellent Li^+ conductivity. Using the Bruce-Vincent method, the Li-ion transference number (t_{Li+}) was determined to be 0.74 at room temperature, significantly outperforming the lithium-ion transport properties of PVDF-HFP and PVP [28, 55-57]. Studies suggest that high cation transference numbers in composite electrolytes with relatively low inorganic filler content can be attributed to these interfacial regions, which play a crucial role in facilitating efficient ion transport [58, 59].

Given the potential hazards posed by lithium dendrite growth, ensuring electrolyte non-flammability is critical for lithium metal batteries (LMBs) safety. As shown in Figure S9, IPE15 did not ignite even after 7 s, whereas PE ignited within 5 seconds and continued burning for the

same duration, and IPE15 was stable up to 15 s. This lower flammability nature of IPE15 plays a key role in enhancing the safety of LMBs. Moreover, IPE15 exhibits broad electrochemical stability up to ~4.58 V, as depicted in Figure 5(b). This stability limit was determined from the onset of a pronounced increase in oxidation current, corresponding to a threshold current density of 10 nA cm^{-2} (I = 25 nA and a = 2.54 cm^2). To further examine the electrochemical stability of IPE15 at high voltage, FTIR spectra of the electrolyte before and after LSV scanning were recorded. The corresponding spectra and detailed peak assignments are provided in the Supplementary Information (Figure S10 and Table S1). A wider electrochemical window enhances safety and stability by providing greater tolerance to overcharging or discharging, thereby minimizing the likelihood of thermal runaway and cell failure.

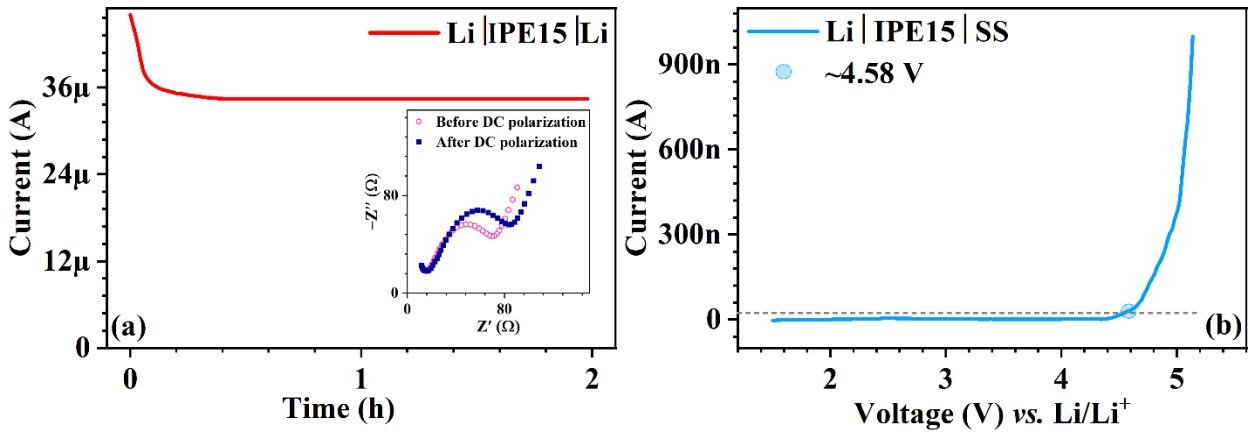

Fig. 5. (a) Chronoamperometry profile and (b) LSV curve of IPE15. Inset (a) shows RT Nyquist plots before and after DC polarization.

To evaluate the compatibility with lithium metal, symmetric Li||Li cells were tested for the stripping/plating process under varying current densities from 0.5 mA cm^{-2} to 5 mA cm^{-2}. As illustrated in Figure 6, the cell demonstrated cycling without short-circuiting at 5 mA cm^{-2} using capacity control techniques (0.25 mAh cm^{-2}). The Li|IPE15|Li cell exhibited stable cycling for over 150 h at 0.5 mA cm^{-2} with low polarization voltage. Additionally, it could operate at 1 and 2

mA cm^{-2} for more than 500 hours, as shown in Figure 6. The Nyquist plot after 500 h of cycling at a current density of 1 mA cm^{-2} is presented in Figure S11. To further investigate SEI stability and its effect on lithium deposition morphology, Li||Cu cells were assembled. As shown in Figure S12, the Li|IPE15|Cu cell achieved 30 cycles with an average Coulombic efficiency of 97.33%. After depositing 0.2 mAh cm^{-2} of lithium on the copper foil, dense and interconnected lithium particles were observed (Figure S13). Additional compatibility testing involved immersing lithium metal in the electrolyte and monitoring surface and electrolyte changes (Figure S14). Even after 50 days, the lithium surface remained unchanged in IPE15, showing no visible surface

degradation. This indicates improved electrolyte compatibility with lithium metal, likely attributed to the development of a durable SEI layer during cycling.

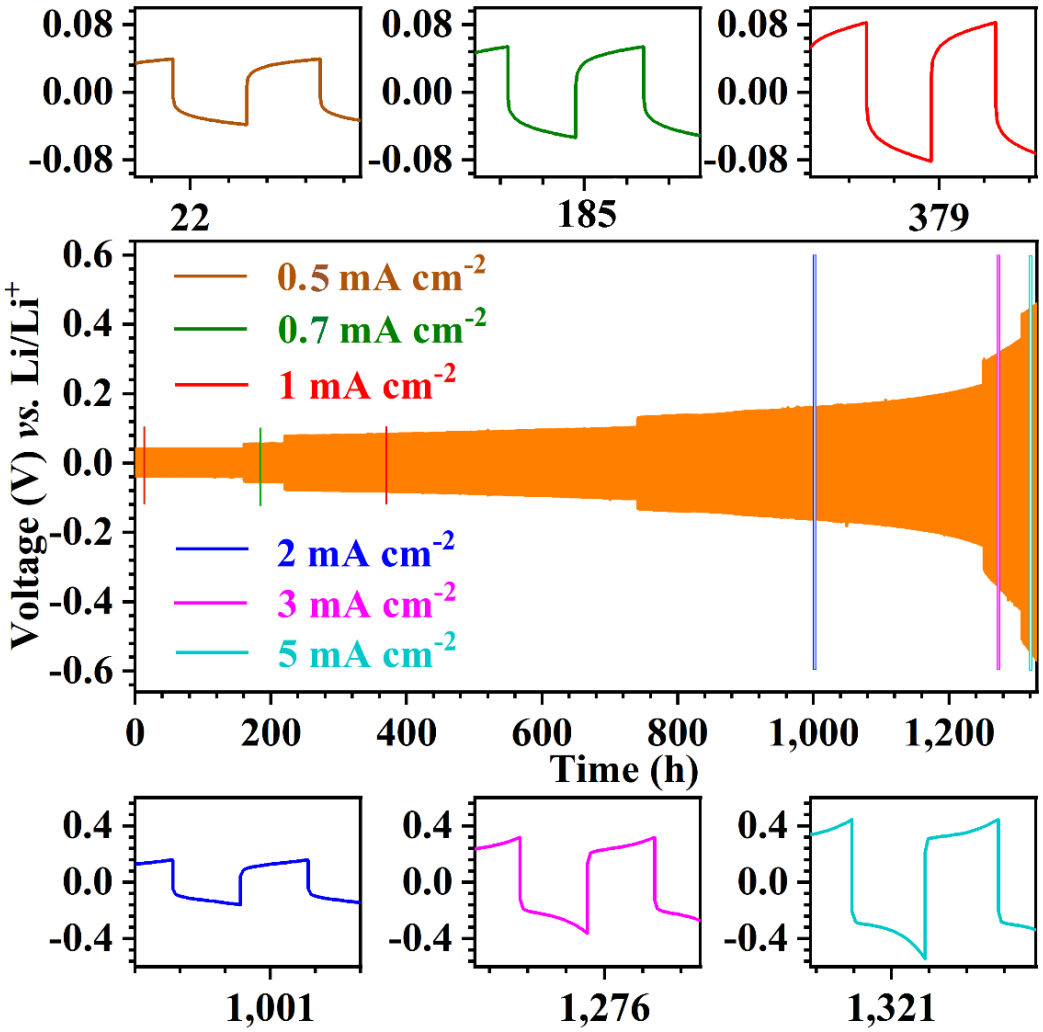

Fig. 6. Galvanostatic cycling profiles of Li|IPE15|Li cell at different current densities at RT.

To further evaluate the effect of the improved interfacial ion transport kinetics on electrochemical performance, Li||LFP full cells were tested under varying operating conditions. The rate capability and corresponding galvanostatic charge/discharge profiles at C-rates ranging from 0.25C to 6C are shown in Figure 7(a-e). A progressive decline in discharge-specific capacity was observed with increasing C-rate, attributable to kinetic limitations in Li-ion diffusion at elevated current densities. Notably, reducing the discharge rate back to 0.25C results in capacity recovery of ~95%. The

dQ/dV vs. V plots represent the differential capacity of the Li/LFP cell as a function of voltage, highlighting the key redox reactions associated with lithium insertion and extraction in the LFP material (Figure 7(c)) [60]. At C/2, the cell delivers a discharge capacity of 142 mAh g^{-1} with capacity retention of 96% after 200 cycles. Remarkably, IPE15 demonstrates excellent rate performance even under high current densities of 4C and 6C, yielding discharge capacities of 77 mAh g^{-1} and 50 mAh g^{-1}, respectively (Fig. 7(b)). IPE15 maintains a capacity retention of 90% after 200 cycles, with an exceptionally stable average Coulombic efficiency of 99.99% at 4C (Fig. 7(d)). While charging at 2C, the LFP‖Li cell with IPE15 retains 78% capacity after 1000 cycles, achieving a high Coulombic efficiency of 99.99% (Fig. 7(e)). Figure S16 displays scanning electron microscopy (SEM) images and X-ray diffraction (XRD) patterns of the LFP cathode surface after 1000 cycles at a 2C rate. The SEM images reveal that the LFP cathode remains free of cracks, while the XRD patterns indicate no signs of by-product.

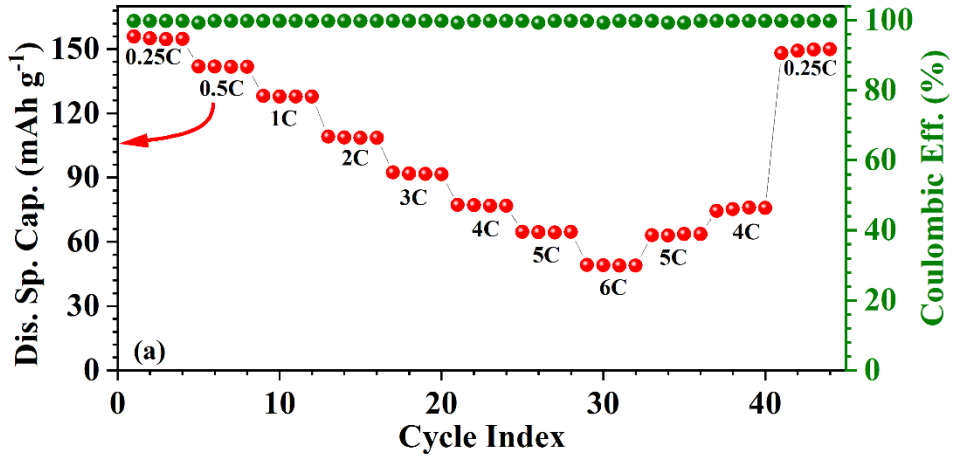
Dis. Sp. Cap. (mAh g-1)
Coulombic Eff. (%)
Cycle Index
0.25C
0.5C
1C
2C
3C
4C
5C
6C
5C
4C
0.25C
(a)

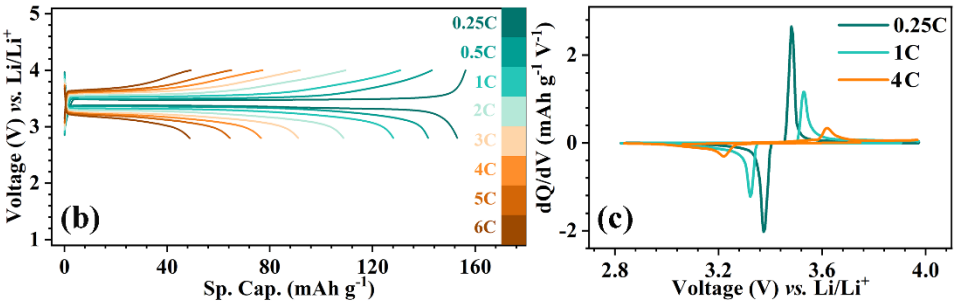
Voltage (V) vs. Li/Li+
Sp. Cap. (mAh g-1)
0.25C
0.5C
1C
2C
3C
4C
5C
6C
(b)
dQ/dV (mAh g-1 V-1)
Voltage (V) vs. Li/Li+
0.25C
1C
4C
(c)

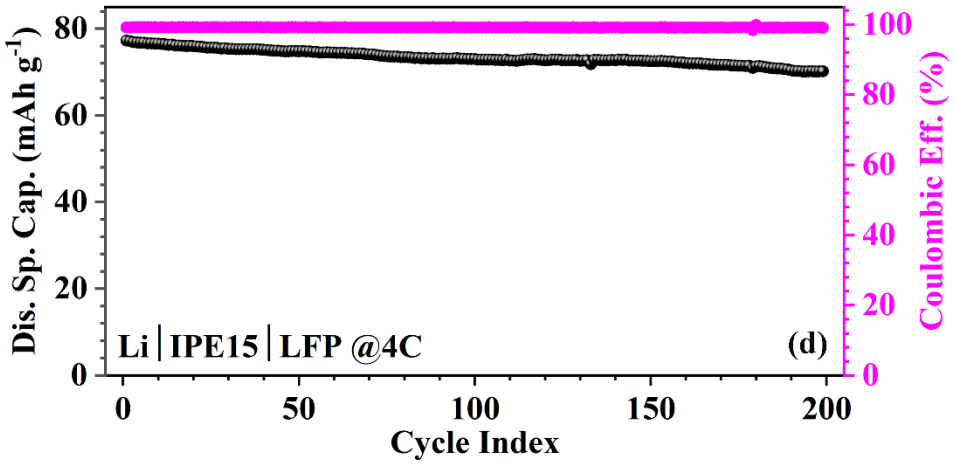
Dis. Sp. Cap. (mAh g-1)
Coulombic Eff. (%)
Cycle Index
Li | IPE15 | LFP @4C
(d)

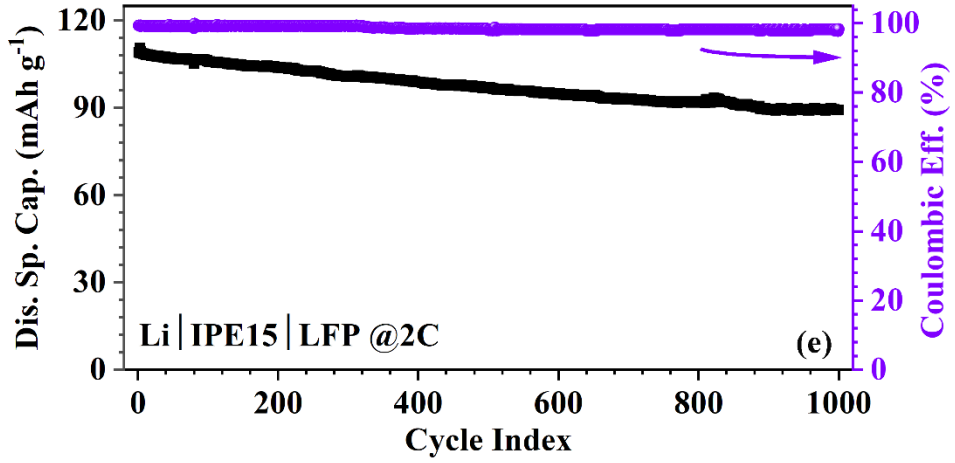
Dis. Sp. Cap. (mAh g-1)
Coulombic Eff. (%)
Cycle Index
Li | IPE15 | LFP @2C
(e)

Fig. 7. Electrochemical performance of the Li|IPE15|LiFePO4 cell: (a) rate performance, (b) RT charge/discharge curves at different C-rates, (c) dQ/dV vs. V plots, and cyclability at (d) 4C and (e) 2C.

As a further step, the performance of the IPE15 electrolyte under high cutoff voltage and at higher temperatures was evaluated. With a higher cutoff voltage of 4.2 V, the Li|IPE15|LFP can still cycle more than 280 times with a capacity retention of ~90.3% at 4C (Figure S17). As shown in Figure S18 at 20 °C, the Li|IPE15|LFP cell discharge capacity of 72.63 mAh g^{-1} can be observed at rates of 2C. Additionally, cycling performance at a high temperature of 80 °C in a cell reveals superior cycling performance with a capacity retention of 93.8% with much lesser polarization (~ 0.12 V) after 20 cycles at 2C (Figure 8). This is attributed to the reduced cell polarization owing to the electrolyte's high thermal stability and increased conductivity at elevated temperatures.

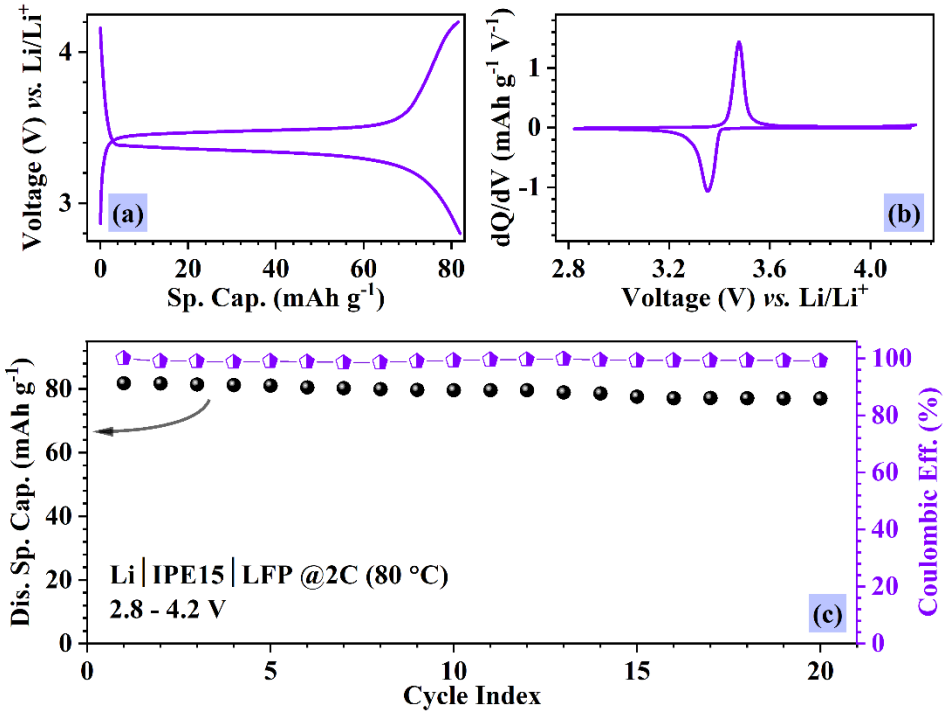

Fig 8. Electrochemical performance of the cell at 80 °C. (a) charge/discharge curve of the Li|IPE15|LFP cell, (b) dQ/dV plot, and (c) cycling stability of the Li||LFP cell at 2C.

3. Conclusions

In this study, a 60 μm thin P(VDF-HFP)-based inorganic polymer electrolyte (IPE) membrane was developed that demonstrated exceptional ion transport capabilities and interfacial stability, making it suitable for practical solid-state lithium metal batteries. By incorporating 15 wt.% inorganic filler ($Li_{1.5}Sn_{1.0}Al_{0.5}Zr_{0.5}(PO_4)_3$) into the polymer blend of poly(vinylidene fluoride hexafluorophosphate) (PVDF-HFP) and polyvinylpyrrolidone (PVP), a room temperature ionic conductivity of 1.48×10^{-4} S cm^{-1}, a Li^+ transference number of 0.74, and electrochemical stability up to 4.58 V was achieved. The symmetric Li|IPE15|Li cell showed stable lithium deposition/stripping over 500 h at 2 mA cm^{-1}, and a full cell with $LiFePO_4$ as the cathode demonstrated over 1000 cycles at 2C. The findings provide an encouraging strategy for developing safe, fast-charging lithium batteries with improved energy density and stability, paving the way for their widespread use in next-generation energy storage technologies.

Declaration of competing interest

The authors declare that they have no known competing financial interests or personal relationships that could have appeared to influence the work reported in this paper.

Acknowledgments

SK thanks the Ministry of Education is also gratefully acknowledged for funding (Grant no. MoE-STARS/STARS-2/2023-0365).

Data availability statement

Data will be made available on request.

References

[1] C.P. Grey, D.S. Hall, Prospects for lithium-ion batteries and beyond—a 2030 vision, Nat. Commun., 11 (2020) 6279. https://doi.org/10.1038/s41467-020-19991-4

[2] A. Manthiram, An Outlook on Lithium Ion Battery Technology, ACS Cent. Sci., 3 (2017) 1063-1069. https://doi.org/10.1021/acscentsci.7b00288

[3] H. Wang, Z. Yu, X. Kong, S.C. Kim, D.T. Boyle, J. Qin, Z. Bao, Y. Cui, Liquid electrolyte: The nexus of practical lithium metal batteries, Joule, 6 (2022) 588-616. https://doi.org/10.1016/j.joule.2021.12.018

[4] Z. Yu, H. Wang, X. Kong, W. Huang, Y. Tsao, D.G. Mackanic, K. Wang, X. Wang, W. Huang, S. Choudhury, Y. Zheng, C.V. Amanchukwu, S.T. Hung, Y. Ma, E.G. Lomeli, J. Qin, Y. Cui, Z. Bao, Molecular design for electrolyte solvents enabling energy-dense and long-cycling lithium metal batteries, Nat. Energy, 5 (2020) 526-533. https://doi.org/10.1038/s41560-020-0634-5

[5] Q. Zhao, S. Stalin, C.-Z. Zhao, L.A. Archer, Designing solid-state electrolytes for safe, energy-dense batteries, Nat. Rev. Mater., 5 (2020) 229-252. https://doi.org/10.1038/s41578-019-0165-5

[6] A. Loutati, O. Guillon, F. Tietz, D. Fattakhova-Rohlfing, NaSICON-type solid-state Li^+ ion conductors with partial polyanionic substitution of phosphate with silicate, Open Ceram., 12 (2022) 100313. https://doi.org/10.1016/j.oceram.2022.100313

[7] S. Xin, Y. You, S. Wang, H.-C. Gao, Y.-X. Yin, Y.-G. Guo, Solid-State Lithium Metal Batteries Promoted by Nanotechnology: Progress and Prospects, ACS Energy Lett., 2 (2017) 1385-1394. https://doi.org/10.1021/acsenergylett.7b00175

[8] S. Shahid, M. Agelin-Chaab, A review of thermal runaway prevention and mitigation strategies for lithium-ion batteries, Energy Convers. Manag. X, 16 (2022) 100310. https://doi.org/10.1016/j.ecmx.2022.100310

[9] Y.-S. Hu, Batteries: getting solid, Nat. Energy, 1 (2016) 1-2. https://doi.org/10.1038/nenergy.2016.42

[10] C. Yang, K. Fu, Y. Zhang, E. Hitz, L. Hu, Protected Lithium-Metal Anodes in Batteries: From Liquid to Solid, Adv Mater, 29 (2017) https://doi.org/10.1002/adma.201701169

[11] L.-Z. Fan, H. He, C.-W. Nan, Tailoring inorganic–polymer composites for the mass production of solid-state batteries, Nat. Rev. Mater., 6 (2021) 1003-1019. https://doi.org/10.1038/s41578-021-00320-0

[12] P. Gami, M. Badole, H.N. Vasavan, A.K. Das, S. Saxena, S. Kumar, Y-Doped $LiZr_2(PO_4)_3$ in a PVDF-HFP Composite Electrolyte for Solid-State Li-Metal Batteries, ACS Appl. Eng. Mater., 2 (2024) 1278-1287. https://doi.org/10.1021/acsaenm.4c00076

[13] A.K. Das, M. Badole, H.N. Vasavan, S. Saxena, P. Gami, S. Deswal, P. Kumar, S. Kumar, Enhancing room temperature performance of solid-state lithium cell via a facile solid electrolyte-cathode interface design, Mater. Today Sustain., 26 (2024) 100758. https://doi.org/10.1016/j.mtsust.2024.100758

[14] P. Yao, H. Yu, Z. Ding, Y. Liu, J. Lu, M. Lavorgna, J. Wu, X. Liu, Review on Polymer-Based Composite Electrolytes for Lithium Batteries, Front. Chem., 7 (2019) https://doi.org/10.3389/fchem.2019.00522

[15] Y. Jiang, K. Chen, J. He, Y. Sun, X. Zhang, X. Yang, H. Xie, J. Liu, A self-healing composite solid electrolyte with dynamic three-dimensional inorganic/organic hybrid network for flexible all-solid-state lithium metal batteries, J Colloid Interface Sci, 678 (2025) 200-209. https://doi.org/10.1016/j.jcis.2024.09.119

[16] J. Lopez, D.G. Mackanic, Y. Cui, Z. Bao, Designing polymers for advanced battery chemistries, Nat. Rev. Mater., 4 (2019) 312-330. https://doi.org/10.1038/s41578-019-0103-6

[17] A.K. Das, M. Badole, H.N. Vasavan, S. Saxena, P. Gami, S. Kumar, Highly conductive ceramic-in-polymer composite electrolyte enabling superior electrochemical performance for all-solid-state lithium batteries, Ceram Int, 49 (2023) 29719-29728. https://doi.org/10.1016/j.ceramint.2023.06.214

[18] P. Gami, A.K. Das, M. Badole, H.N. Vasavan, S. Saxena, N. Dagar, S. Deswal, P. Kumar, A. Dwivedi, H.K. Poswal, S. Kumar, Fostering Li-ion conduction in Zr-Sn-Al-based mid-entropy NASICON electrolyte, Ceram Int, 50 (2024) 47612-47619. https://doi.org/10.1016/j.ceramint.2024.09.107

[19] K. Chen, J. Liu, X. Zhang, Y. Sun, H. Xie, Three-dimensional cross-linked network deep eutectic gel polymer electrolyte with the self-healing ability enable by hydrogen bonds and dynamic disulfide bonds, J Colloid Interface Sci, 669 (2024) 529-536. https://doi.org/10.1016/j.jcis.2024.05.015

[20] Y. Sun, M. Wang, X. Zhang, H. Xie, J. Liu, Additive-free nitrile-based gel polymer electrolytes with enhanced interfacial compatibility for Lithium metal batteries, Chem Eng J, 519 (2025) 165528. https://doi.org/10.1016/j.cej.2025.165528

[21] A.K. Das, M. Badole, H.N. Vasavan, S. Saxena, P. Gami, N. Dagar, S. Kumar, $LiTa_2PO_8$-Based Polymer–Ceramic Electrolyte Paved the Way to High-Performance Solid-State Lithium Metal Batteries, Energy Fuels, 38 (2024) 11253-11261. https://doi.org/10.1021/acs.energyfuels.4c01520

[22] Y.-G. Lee, S. Fujiki, C. Jung, N. Suzuki, N. Yashiro, R. Omoda, D.-S. Ko, T. Shiratsuchi, T. Sugimoto, S. Ryu, J.H. Ku, T. Watanabe, Y. Park, Y. Aihara, D. Im, I.T. Han, High-energy long-cycling all-solid-state lithium metal batteries enabled by silver–carbon composite anodes, Nat. Energy, 5 (2020) 299-308. https://doi.org/10.1038/s41560-020-0575-z

[23] J. Guo, H. Xu, Y. Sun, K. Chen, X. Zhang, H. Xie, Y. Jiang, J. Liu, Borate-containing triblock copolymer electrolytes for improved lithium-ion transference number and interface stability, J Colloid Interface Sci, 660 (2024) 565-573. https://doi.org/10.1016/j.jcis.2024.01.097

[24] Y. Su, X. Rong, A. Gao, Y. Liu, J. Li, M. Mao, X. Qi, G. Chai, Q. Zhang, L. Suo, L. Gu, H. Li, X. Huang, L. Chen, B. Liu, Y.-S. Hu, Rational design of a topological polymeric solid electrolyte for high-performance all-solid-state alkali metal batteries, Nat. Commun., 13 (2022) 4181. https://doi.org/10.1038/s41467-022-31792-5

[25] R. Lin, Y. He, C. Wang, P. Zou, E. Hu, X.-Q. Yang, K. Xu, H.L. Xin, Characterization of the structure and chemistry of the solid–electrolyte interface by cryo-EM leads to high-performance solid-state Li-metal batteries, Nat. Nanotechnol., 17 (2022) 768-776. https://doi.org/10.1038/s41565-022-01148-7

[26] N. Kim, S. Chae, J. Ma, M. Ko, J. Cho, Fast-charging high-energy lithium-ion batteries via implantation of amorphous silicon nanolayer in edge-plane activated graphite anodes, Nat. Commun., 8 (2017) 812. https://doi.org/10.1038/s41467-017-00973-y

[27] Y. Ma, R. Shang, Y. Liu, R. Lake, M. Ozkan, C.S. Ozkan, Enabling fast-charging capability for all-solid-state lithium-ion batteries, J Power Sources, 559 (2023) 232647. https://doi.org/10.1016/j.jpowsour.2023.232647

[28] J. B, A. Km, M. M, P. V.S, J. S, Development of a novel type of solid polymer electrolyte for solid state lithium battery applications based on lithium enriched poly (ethylene oxide) (PEO)/poly (vinyl pyrrolidone) (PVP) blend polymer, Electrochim Acta, 235 (2017) 210-222. https://doi.org/10.1016/j.electacta.2017.03.118

[29] K. Karpagavel, K. Sundaramahalingam, A. Manikandan, D. Vanitha, A. Manohar, E.R. Nagarajan, N. Nallamuthu, Electrical Properties of Lithium-Ion Conducting Poly (Vinylidene

Fluoride-Co-Hexafluoropropylene) (PVDF-HFP)/Polyvinylpyrrolidone (PVP) Solid Polymer Electrolyte, J Electron Mater, 50 (2021) 4415-4425. https://doi.org/10.1007/s11664-021-08967-9

[30] H. Feng, Z. Feng, L. Shen, A high resolution solid-state n.m.r. and d.s.c. study of miscibility and crystallization behaviour of poly(vinyl alcohol)poly(N-vinyl-2-pyrrolidone) blends, Polymer, 34 (1993) 2516-2519. https://doi.org/10.1016/0032-3861(93)90581-T

[31] A.R. Polu, R. Kumar, H.-W. Rhee, Magnesium ion conducting solid polymer blend electrolyte based on biodegradable polymers and application in solid-state batteries, Ionics, 21 (2015) 125-132. https://doi.org/10.1007/s11581-014-1174-4

[32] K. Kesavan, C.M. Mathew, S. Rajendran, M. Ulaganathan, Preparation and characterization of novel solid polymer blend electrolytes based on poly (vinyl pyrrolidone) with various concentrations of lithium perchlorate, Mater. Sci. Eng. B, 184 (2014) 26-33. https://doi.org/10.1016/j.mseb.2014.01.009

[33] H. Zhang, C. Liu, L. Zheng, F. Xu, W. Feng, H. Li, X. Huang, M. Armand, J. Nie, Z. Zhou, Lithium bis(fluorosulfonyl)imide/poly(ethylene oxide) polymer electrolyte, Electrochim Acta, 133 (2014) 529-538. https://doi.org/10.1016/j.electacta.2014.04.099

[34] Y.-F. Huang, T. Gu, G. Rui, P. Shi, W. Fu, L. Chen, X. Liu, J. Zeng, B. Kang, Z. Yan, F.J. Stadler, L. Zhu, F. Kang, Y.-B. He, A relaxor ferroelectric polymer with an ultrahigh dielectric constant largely promotes the dissociation of lithium salts to achieve high ionic conductivity, EES, 14 (2021) 6021-6029. https://doi.org/10.1039/D1EE02663A

[35] F. Zheng, M. Kotobuki, S. Song, M.O. Lai, L. Lu, Review on solid electrolytes for all-solid-state lithium-ion batteries, J Power Sources, 389 (2018) 198-213. https://doi.org/10.1016/j.jpowsour.2018.04.022

[36] X. Zhang, J. He, Y. Sun, H. Xie, J. Liu, Enhanced inorganic-organic interphase compatibility in composite solid electrolytes by forming isocyanate-linked hybrid cross-linked networks, J Colloid Interface Sci, 700 (2025) 138441. https://doi.org/10.1016/j.jcis.2025.138441

[37] S. Jin, X. Gao, S. Hong, Y. Deng, P. Chen, R. Yang, Y.L. Joo, L.A. Archer, Fast-charge, long-duration storage in lithium batteries, Joule, 8 (2024) 746-763. https://doi.org/10.1016/j.joule.2023.12.022

[38] Y. Liu, Y. Zhu, Y. Cui, Challenges and opportunities towards fast-charging battery materials, Nat. Energy, 4 (2019) 540-550. https://doi.org/10.1038/s41560-019-0405-3

[39] W. Cai, Y.-X. Yao, G.-L. Zhu, C. Yan, L.-L. Jiang, C. He, J.-Q. Huang, Q. Zhang, A review on energy chemistry of fast-charging anodes, Chem Soc Rev, 49 (2020) 3806-3833. https://doi.org/10.1039/C9CS00728H

[40] J. Yu, Y. Wang, L. Shen, J. Liu, Z. Wang, S. Xu, H.M. Law, F. Ciucci, Fast-Charging Solid-State Li Batteries: Materials, Strategies, and Prospects, Adv Mater, (2024) e2417796. https://doi.org/10.1002/adma.202417796

[41] U. Gradišar Centa, M. Mihelčič, V. Bobnar, M. Remškar, L. Slemenik Perše, The Effect of PVP on Thermal, Mechanical, and Dielectric Properties in PVDF-HFP/PVP Thin Film, Coatings, 12 (2022) 1241. https://doi.org/10.3390/coatings12091241

[42] P. Gami, M. Badole, H.N. Vasavan, A.K. Das, S. Saxena, N. Dagar, V. Srihari, S. Kumar, NASICON-type medium entropy $Li_{1.5}Sn_{1.0}Al_{0.5}Zr_{0.5}(PO_4)_3$ electrolyte for solid state Li metal batteries, J Power Sources, 618 (2024) 235214. https://doi.org/10.1016/j.jpowsour.2024.235214

[43] C. Luo, M. Yi, Z. Cao, W. Hui, Y. Wang, Review of Ionic Conductivity Properties of NASICON Type Inorganic Solid Electrolyte LATP, ACS Appl. Electron. Mater., 6 (2024) 641-657. https://doi.org/10.1021/acsaelm.3c01747

[44] J. Xiao, B. Zhang, J. Liu, X. He, Z. Xiao, H. Qin, T. Liu, K. Amine, X. Ou, NaSICON-type materials for lithium-ion battery applications: Progress and challenges, Nano Energy, 127 (2024) 109730. https://doi.org/10.1016/j.nanoen.2024.109730

[45] I.S. Elashmawi, E.M. Abdelrazek, A.Y. Yassin, Influence of $NiCl_2/CdCl_2$ as Mixed Filler on Structural, Thermal and Electrical Properties of PVA/PVP Blend, CJAST, 4 (2014) 4263-4279. https://doi.org/10.9734/BJAST/2014/12317

[46] B. Kumar, L.G. Scanlon, Polymer-ceramic composite electrolytes, J Power Sources, 52 (1994) 261-268. https://doi.org/10.1016/0378-7753(94)02147-3

[47] W. Liu, N. Liu, J. Sun, P.-C. Hsu, Y. Li, H.-W. Lee, Y. Cui, Ionic Conductivity Enhancement of Polymer Electrolytes with Ceramic Nanowire Fillers, Nano Lett, 15 (2015) 2740-2745. https://doi.org/10.1021/acs.nanolett.5b00600

[48] A. Manuel Stephan, K.S. Nahm, Review on composite polymer electrolytes for lithium batteries, Polymer, 47 (2006) 5952-5964. https://doi.org/10.1016/j.polymer.2006.05.069

[49] S. Mogurampelly, V. Ganesan, Influence of nanoparticle surface chemistry on ion transport in polymer nanocomposite electrolytes, Solid State Ion., 286 (2016) 57-65. https://doi.org/10.1016/j.ssi.2015.12.018

[50] B. Hanson, V. Pryamitsyn, V. Ganesan, Mechanisms Underlying Ionic Mobilities in Nanocomposite Polymer Electrolytes, ACS Macro Lett., 2 (2013) 1001-1005. https://doi.org/10.1021/mz400234m

[51] K. Deshmukh, M.B. Ahamed, A.R. Polu, K.K. Sadasivuni, S.K.K. Pasha, D. Ponnamma, M.A.-A. AlMaadeed, R.R. Deshmukh, K. Chidambaram, Impedance spectroscopy, ionic conductivity and dielectric studies of new Li^+ ion conducting polymer blend electrolytes based on

biodegradable polymers for solid state battery applications, J. Mater. Sci.: Mater. Electron., 27 (2016) 11410-11424. https://doi.org/10.1007/s10854-016-5267-x

[52] M. Jia, M. Khurram Tufail, X. Guo, Insight into the Key Factors in High Li^+ Transference Number Composite Electrolytes for Solid Lithium Batteries, ChemSusChem, 16 (2023) e202201801. https://doi.org/10.1002/cssc.202201801

[53] F.P. Nkosi, I. Cuevas, M. Valvo, J. Mindemark, A. Mahun, S. Abbrent, J. Brus, L. Kobera, K. Edström, Understanding Lithium-Ion Conductivity in NASICON-Type Polymer-in-Ceramic Composite Electrolytes, ACS Appl. Energy Mater., 7 (2024) 4609-4619. https://doi.org/10.1021/acsaem.4c00701

[54] Z. Li, H.-M. Huang, J.-K. Zhu, J.-F. Wu, H. Yang, L. Wei, X. Guo, Ionic Conduction in Composite Polymer Electrolytes: Case of PEO:Ga-LLZO Composites, ACS Appl. Mater. Interfaces., 11 (2019) 784-791. https://doi.org/10.1021/acsami.8b17279

[55] W. Liu, X.K. Zhang, F. Wu, Y. Xiang, A study on PVDF-HFP gel polymer electrolyte for lithium-ion batteries, IOP Conf. Ser.: Mater. Sci. Eng., 213 (2017) 012036. https://doi.org/10.1088/1757-899X/213/1/012036

[56] Z. Yao, F. Qi, L. Ye, Q. Sun, X. Gu, X. Yang, K. Zhu, Composite polymer electrolyte based on poly(vinylidene fluoride-hexafluoropropylene) (PVDF-HFP) for solid-state batteries, Heliyon, 10 (2024) e28097. https://doi.org/10.1016/j.heliyon.2024.e28097

[57] P. Zhang, R. Li, J. Huang, B. Liu, M. Zhou, B. Wen, Y. Xia, S. Okada, Flexible poly(vinylidene fluoride-co-hexafluoropropylene)-based gel polymer electrolyte for high-performance lithium-ion batteries, RSC Adv., 11 (2021) 11943-11951. https://doi.org/10.1039/D1RA01250A

[58] W. Wang, E. Yi, A.J. Fici, R.M. Laine, J. Kieffer, Lithium Ion Conducting Poly(ethylene oxide)-Based Solid Electrolytes Containing Active or Passive Ceramic Nanoparticles, J. Phys. Chem. C, 121 (2017) 2563-2573. https://doi.org/10.1021/acs.jpcc.6b11136

[59] C.-W. Nan, L. Fan, Y. Lin, Q. Cai, Enhanced Ionic Conductivity of Polymer Electrolytes Containing Nanocomposite SiO_2 Particles, PRL, 91 (2003) 266104. https://doi.org/10.1103/PhysRevLett.91.266104

[60] A. Fly, R. Chen, Rate dependency of incremental capacity analysis (dQ/dV) as a diagnostic tool for lithium-ion batteries, J. Energy Storage, 29 (2020) 101329. https://doi.org/10.1016/j.est.2020.101329

[Supplementary Materials]

High-Performance Composite Electrolytes for Solid-State Lithium Metal Batteries: Enhancing Ionic Conductivity and Interfacial Compatibility through Polyvinylpyrrolidone Blending and Inorganic Filler Incorporation

Pratiksha Gami and Sunil Kumar*

Department of Metallurgical Engineering and Materials Science, Indian Institute of Technology Indore, Simrol, 453552, India.

*Corresponding author, E-mail: sunil@iiti.ac.in

Experimental Section

LiTFSI, PVP, PVDF-HFP, and DMF were utilized in their as-received state. The 1:3 molar ratio of LiTFSI to PVP/PVDF-HFP (PE) was chosen as it provides the optimal ionic conductivity [1]. The fabrication process of the mid-entropy filler $Li_{1.5}Sn_{1.0}Al_{0.5}Zr_{0.5}(PO_4)_3$ is detailed in our publication [2]. Careful experimental measurements of various PE/$Li_{1.5}Sn_{1.0}Al_{0.5}Zr_{0.5}(PO_4)_3$ weight ratios, ranging from 5 wt.% to 20 wt.%, identified 15 wt.% as the optimal ratio to achieve the optimum conductivity. Fine adjustment of the ratio is crucial for tailoring the electrolyte characteristics.

The cathode slurry was prepared by suspending $LiFeO_4$, Super P, and polyvinylidene fluoride (8:1:1) in N-methylpyrrolidone. This slurry was uniformly cast onto aluminum foil using an automated coating system, followed by drying at 80 °C for 3 h. The resulting electrode sheet was then punched into 13 mm discs.

Materials characterizations

The crystalline structure of the IPE*x* films was examined by X-ray diffraction (XRD) using a Malvern Panalytical Empyrean diffractometer. Data were recorded over a 2θ range of 10-60° with a step size of 0.02°. Fourier-transform infrared (FTIR) spectra of the solid polymer membranes were collected using a PerkinElmer Spectrum Two instrument over the range 4000-400 cm^{-1}. The surface morphology of the electrolyte films was evaluated *via* field-emission scanning electron microscopy (FE-SEM, JEOL-7610+). Elemental distribution within the synthesized samples was further analyzed through energy-dispersive X-ray spectroscopy (EDS).

The ionic conductivity of the electrolyte was determined using complex impedance spectroscopy (CIS) with an impedance analyzer (BioLogic SP-50e). Impedance data were measured out across

a frequency range of 1 MHz to 1 Hz. The conductivity (σ) was calculated using the following equation:

$$\sigma = \frac{1}{R} \times \frac{d}{A} \quad (1)$$

Where d is the membrane thickness, R is the resistance value obtained from fitting of the impedance data, and A is the membrane area. The total ionic conductivity (σ) of the PE incorporating 15 wt% inorganic filler was evaluated as a function of temperature, and the resulting data were fitted using the Arrhenius model.

The thermal behavior of the SPE films was examined through thermogravimetric analysis (TGA) using an STA 8000 instrument. The samples were heated from ambient temperature up to 700 °C under a nitrogen flow to assess their thermal stability. The electrolyte membrane's temperature-dependent storage modulus (E') was evaluated using a DMA 8000 (PerkinElmer) instrument. The sample was initially stabilized at 30 °C, then heated to 130 °C at a 2 °C per min rate.

Using the Keithley Source Meter Unit (model 2450-EC), the electrochemical stability window and the Li^+ transference number were calculated. The Bruce-Vincent method was employed to calculate the transference number of lithium ions (t_{Li+}) in a Li||Li cell configuration. A constant voltage of 0.5 mV was imposed on the cell, and the decay in current was recorded over time until a steady state was achieved (~2 h in this study). Electrochemical impedance spectroscopy (EIS) was conducted before and after polarization to determine the interfacial resistance. The Li^+ transference number (t_{Li+}) was then estimated using the following equation:

$$t_{Li^+} = \frac{I_{ss}(\Delta V - I_o R_o)}{I_o(\Delta V - I_{ss} R_{ss})} \quad (2)$$

Here, I_o refers to the initial current, while I_{ss} corresponds to the steady-state current, while ΔV is the constant applied voltage. The interfacial resistances R_0 and R_{SS} were determined from

impedance data recorded before and after polarization, respectively. The electrolyte's electrochemical stability was probed using LSV with a Li||stainless steel (2032) coin cell at a scan rate of 0.1 mV s^{-1}.

Galvanostatic cycling data was measured using a Neware system. The current density for lithium plating and stripping ranged from 0.5 - 5 mA cm^{-2} with a 0.25 mAh cm^{-2} capacity. Li||Cu cells were fabricated, and the morphology of the lithium deposition was analyzed after the cell was decrimped following cycling. LFP||Li coin cells were fabricated in a controlled environment using the CR2032 configuration. Lithium metal foils, with a diameter of 16 mm, were used as received. Galvanostatic cycling tests were carried out for the LFP electrodes in lithium metal batteries (LMBs) at room temperature (30 °C), 20 °C, and 80 °C.

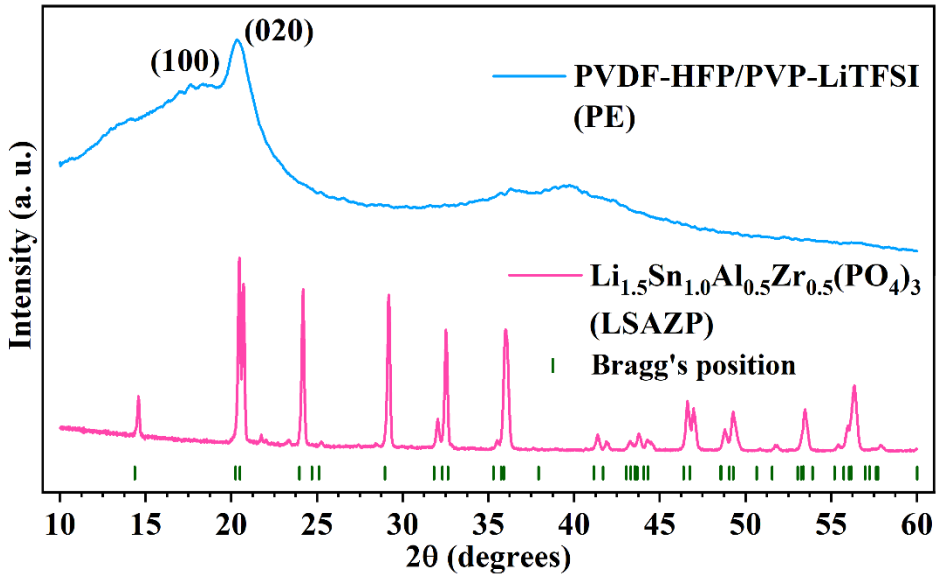

Fig. S1. XRD patterns of polymer blend/salt complex and LSAZP ceramic powder with vertical olive bars indicating the Bragg positions for the rhombohedral space group $R\bar{3}c$.

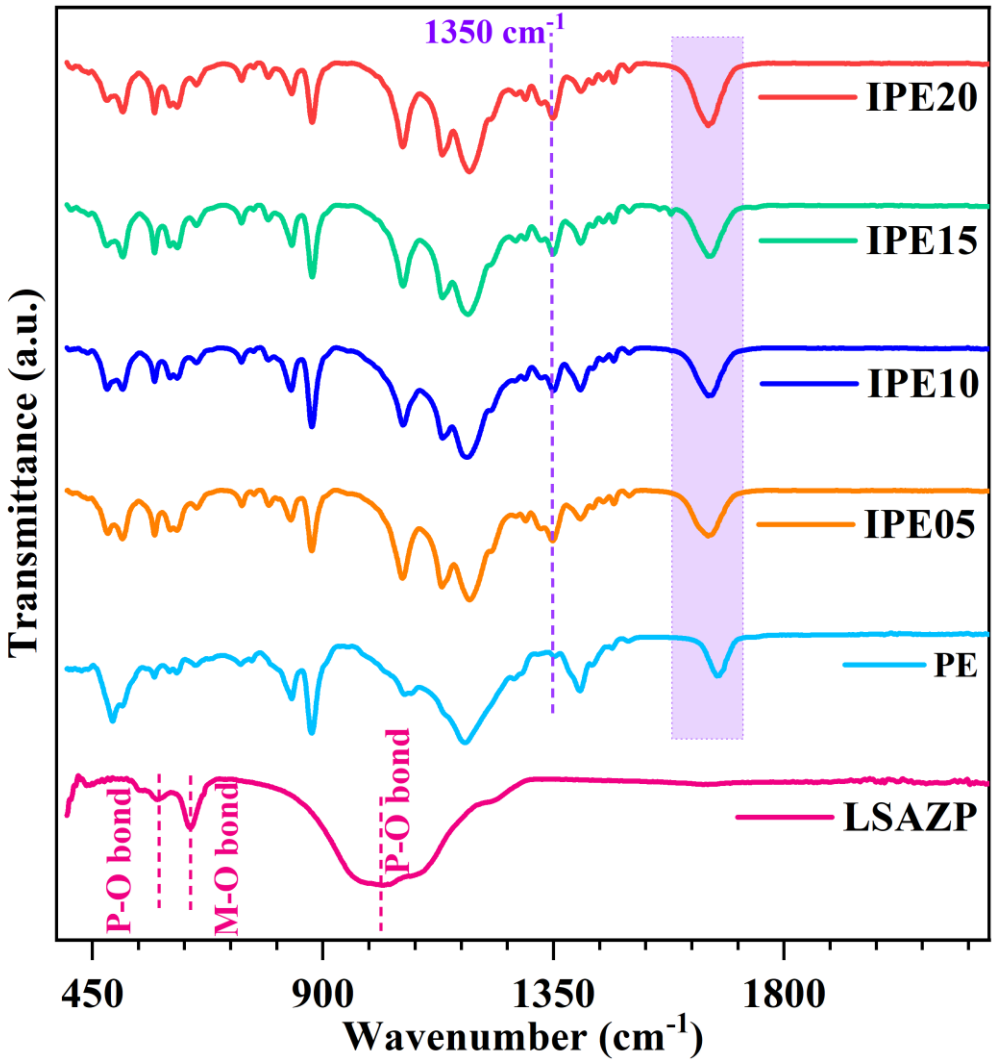

Fig. S2. FT-IR spectra of LSAZP, PE, IPE05, IPE10, IPE15, and IPE20. The light violet regions of the plot highlight H-bonding/dipole-dipole interactions between the ceramic-polymer moieties.

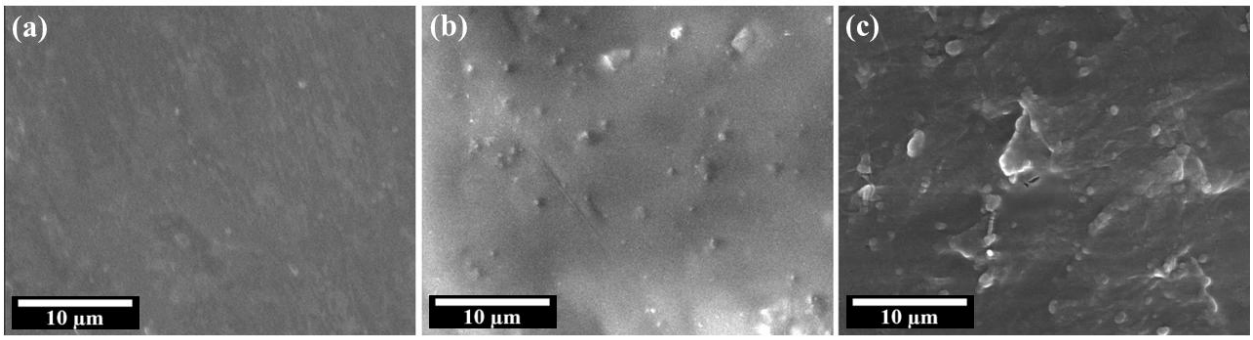

Fig. S3. SEM images of (a) IPE05, (b) IPE10, and (c) IPE20 membranes.

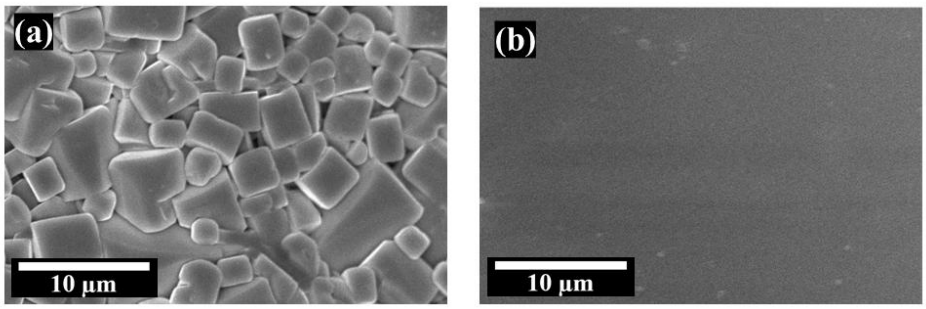

Fig. S4. SEM images of (a) LSAZP and (b) PE samples.

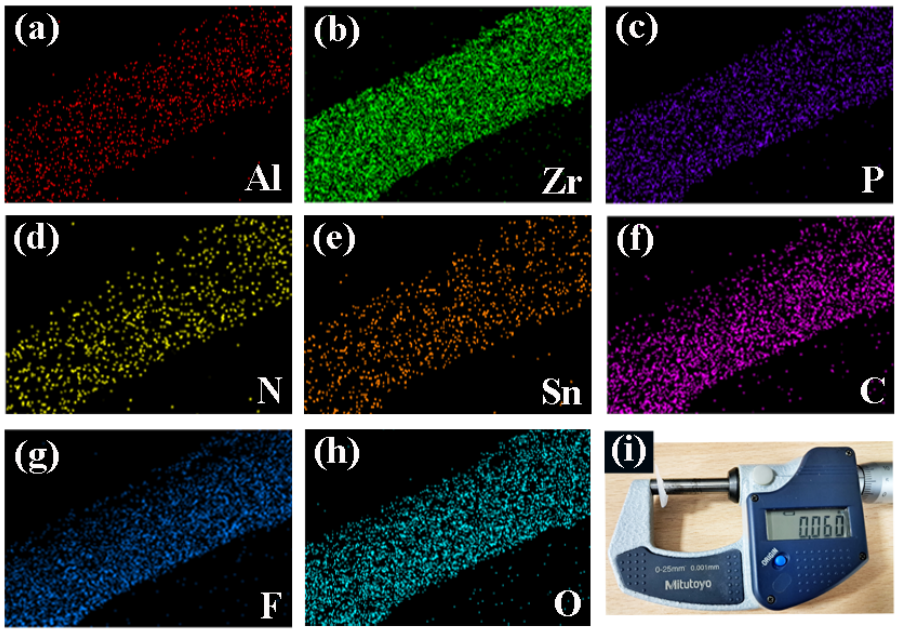

Fig. S5. EDS elemental mappings (a-h) and thickness measurement (i) of IPE15 membrane.

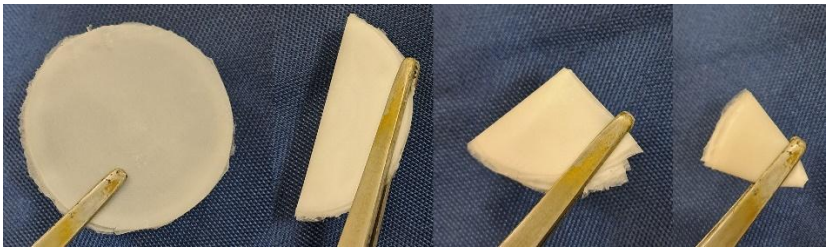

Fig. S6. Foldability test: photographs of IPE15 electrolyte.

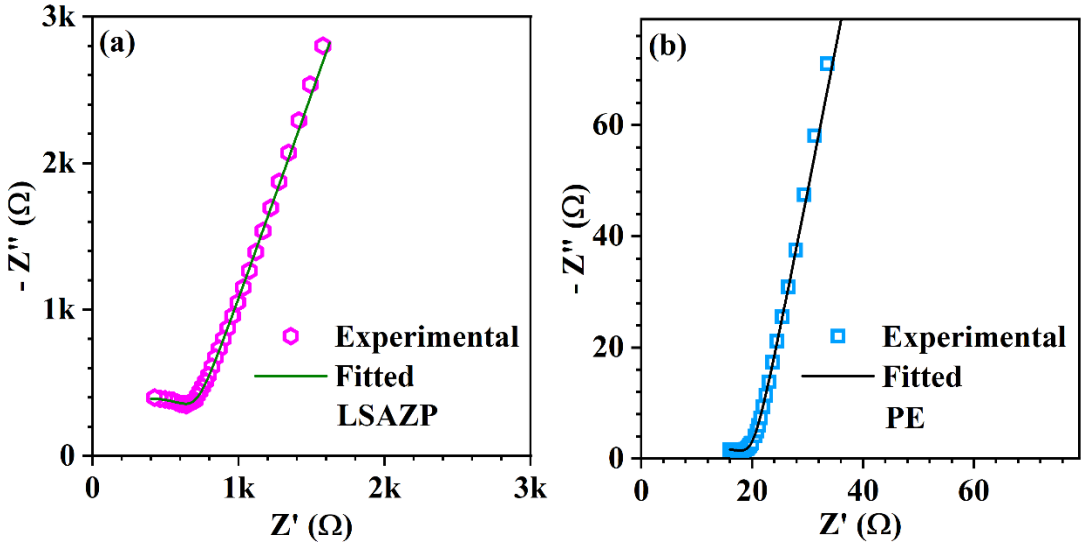

Fig. S7. RT Nyquist plots of (a) LSAZP and (b) PE samples. The experimental data is fitted with the equivalent circuit *(R1||CPE1) + (CPE2).*

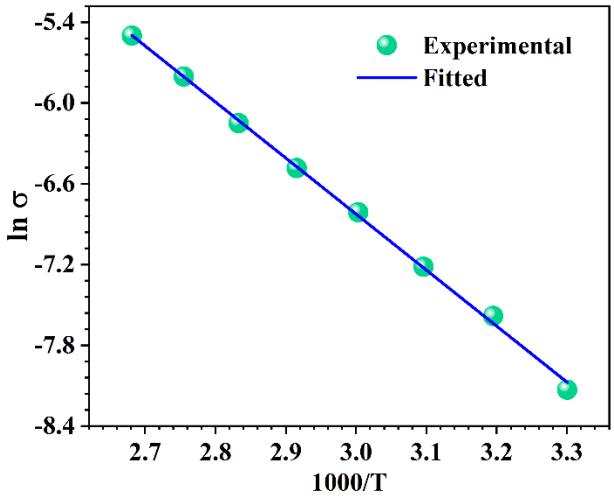

Fig. S8. ln σ *vs.* 1000/T plot of the IPE15 film.

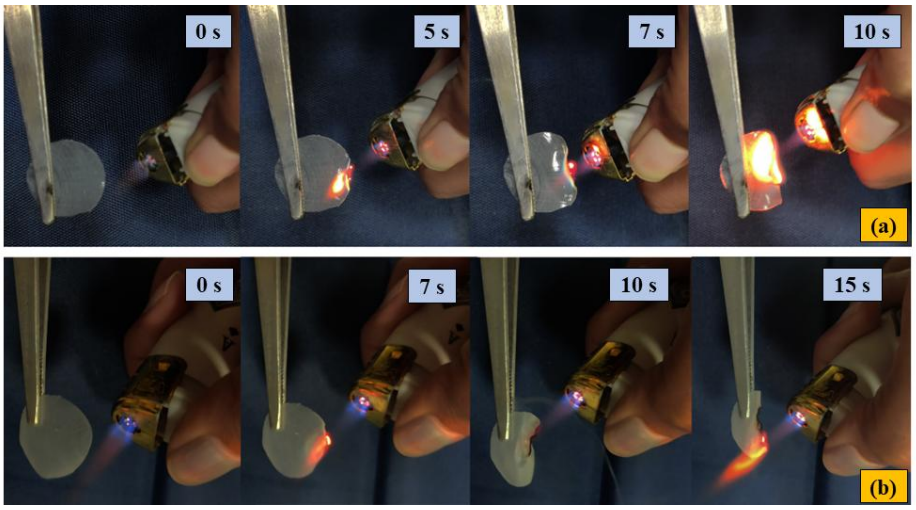

Fig. S9. Images of ignition test for (a) PE and (b) IPE15 electrolytes at various intervals.

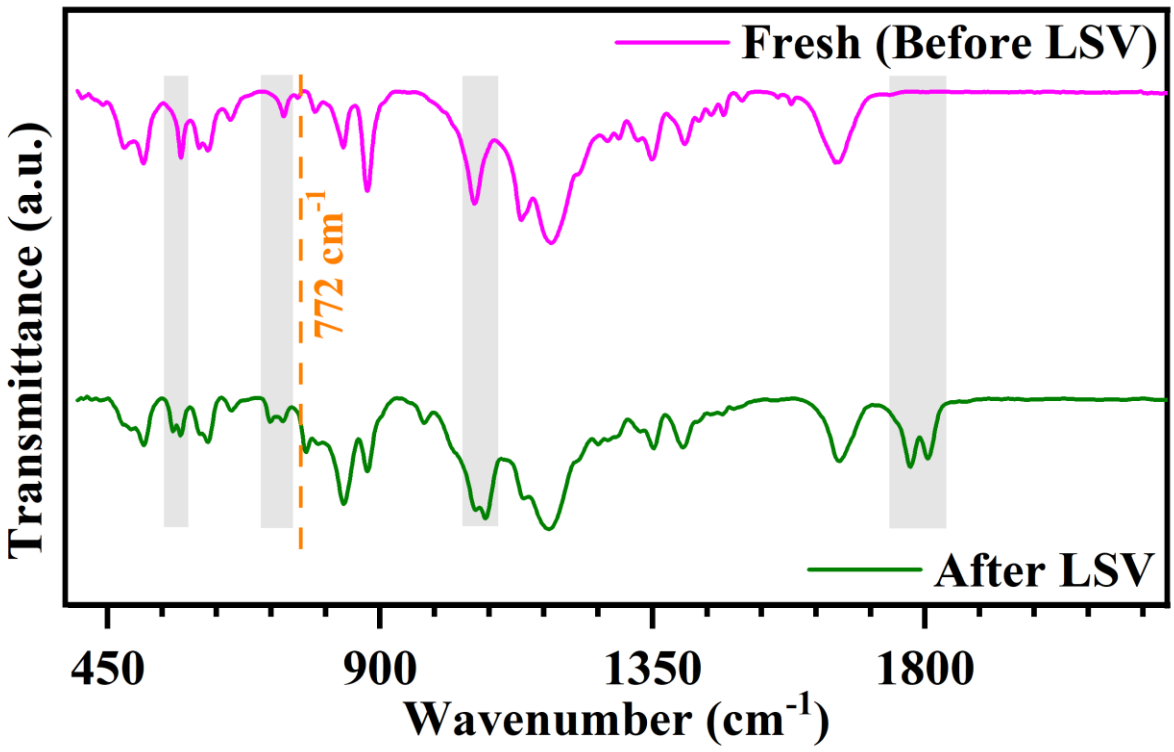

Fig. S10. FTIR spectra of the IPE15 electrolyte before and after LSV scanning; corresponding peak assignments are provided in Table S1.

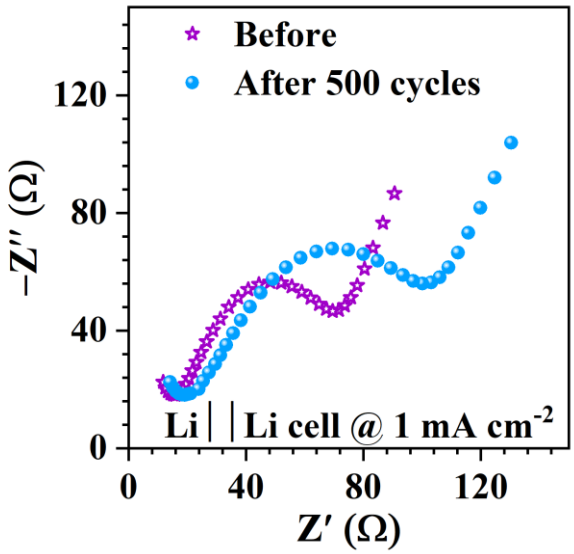

Fig. S11 Nyquist plots of the Li‖IPE15‖Li cell at room temperature before and after 500 h cycling at 1 mA cm^{-2}.

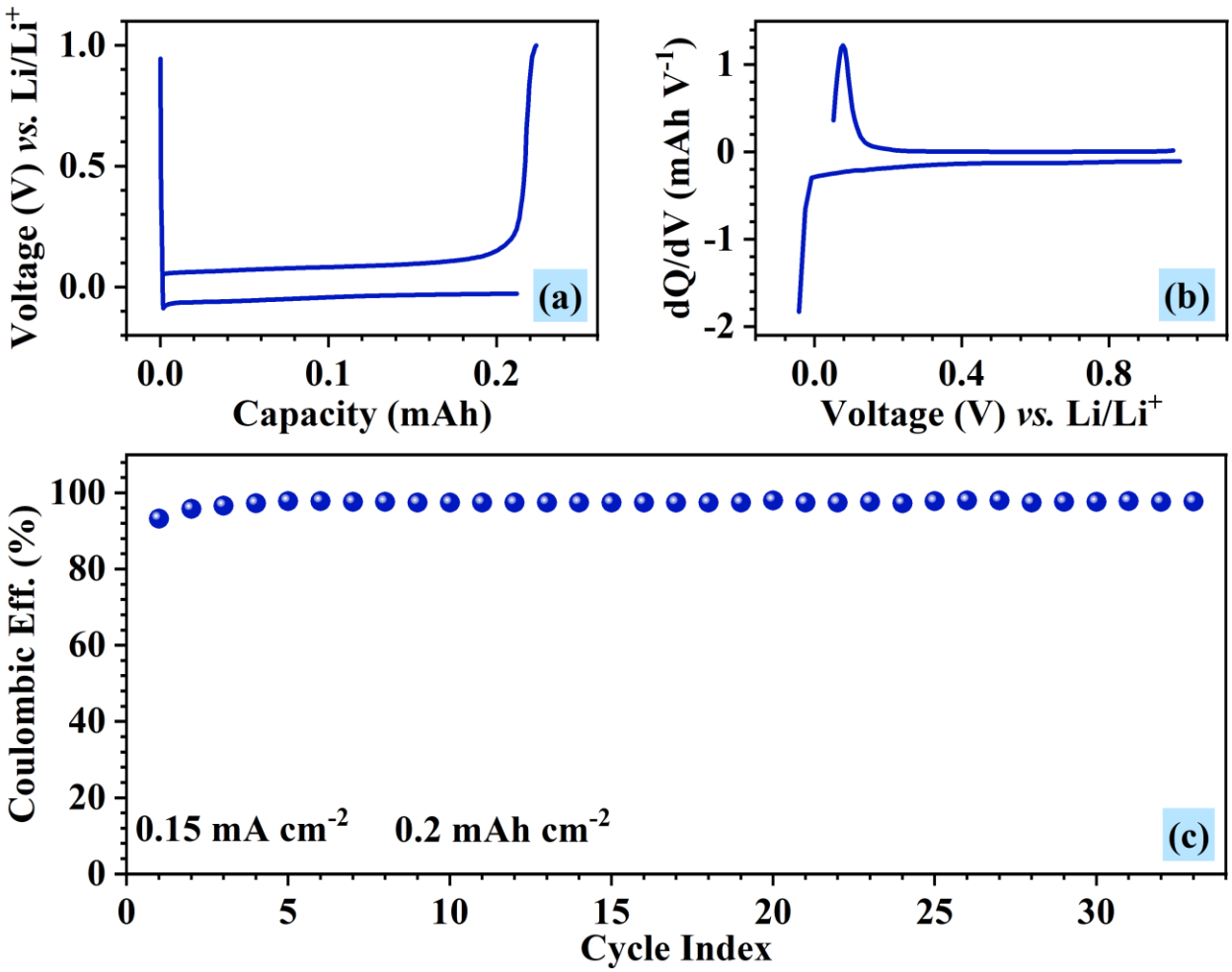

Fig. S12. Li metal compatibility tests of Li||Cu cells using the IPE15 electrolyte. (a) Li deposition-stripping curve, (b) dQ/dV curve, and (c) the corresponding Coulombic efficiency (Eff.) with cycle index.

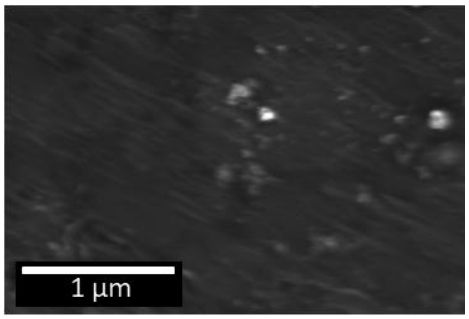

Fig. S13. SEM image of the Li on Cu substrate at 0.15 mA cm^{-2} in Li||Cu cells using IPE15 electrolyte.

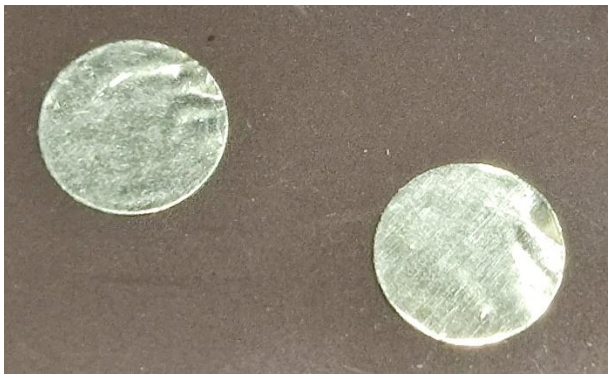

Fig. S14. Image of Li metal before (left) and after (right) contact with IPE15.

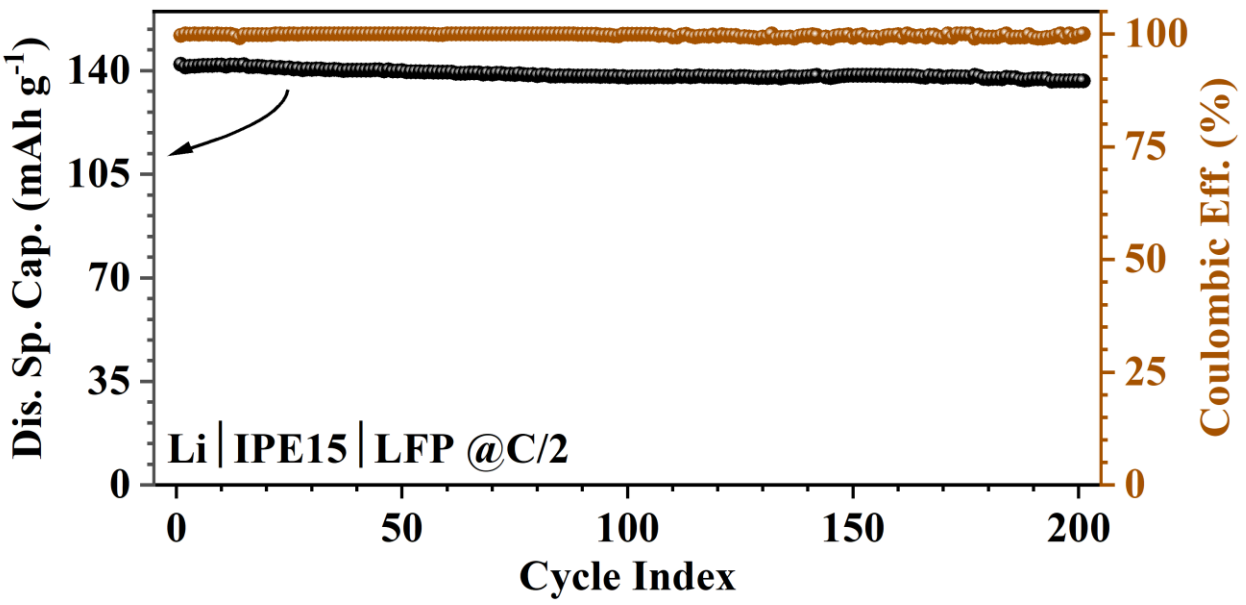

Fig. S15. Long-term cycling stability of IPE15 electrolyte Li||LFP cell at C/2, RT.

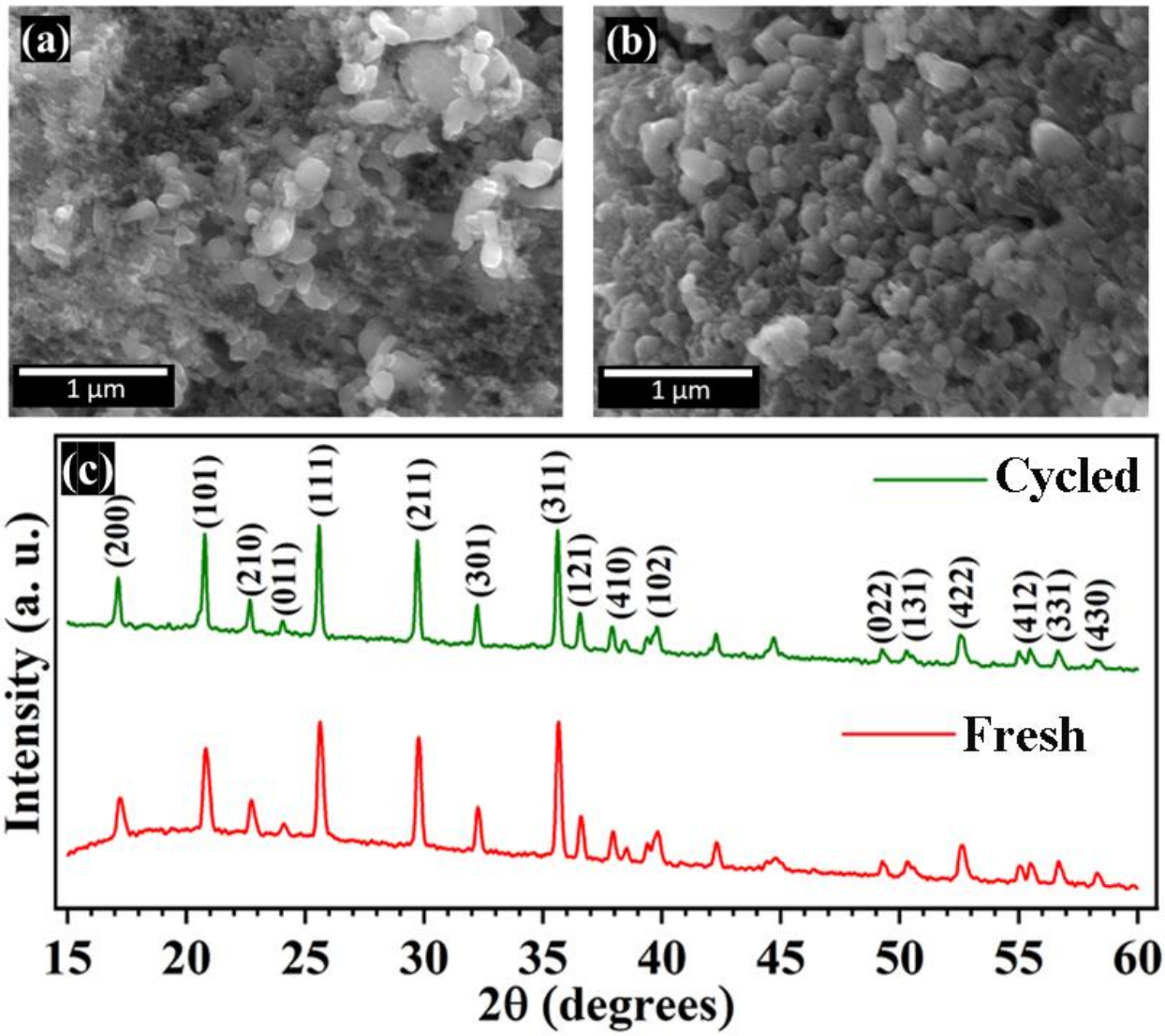

Fig. S16. SEM images of (a) fresh and (b) cycled LFP cathodes, and (c) XRD patterns of LFP after cycling.

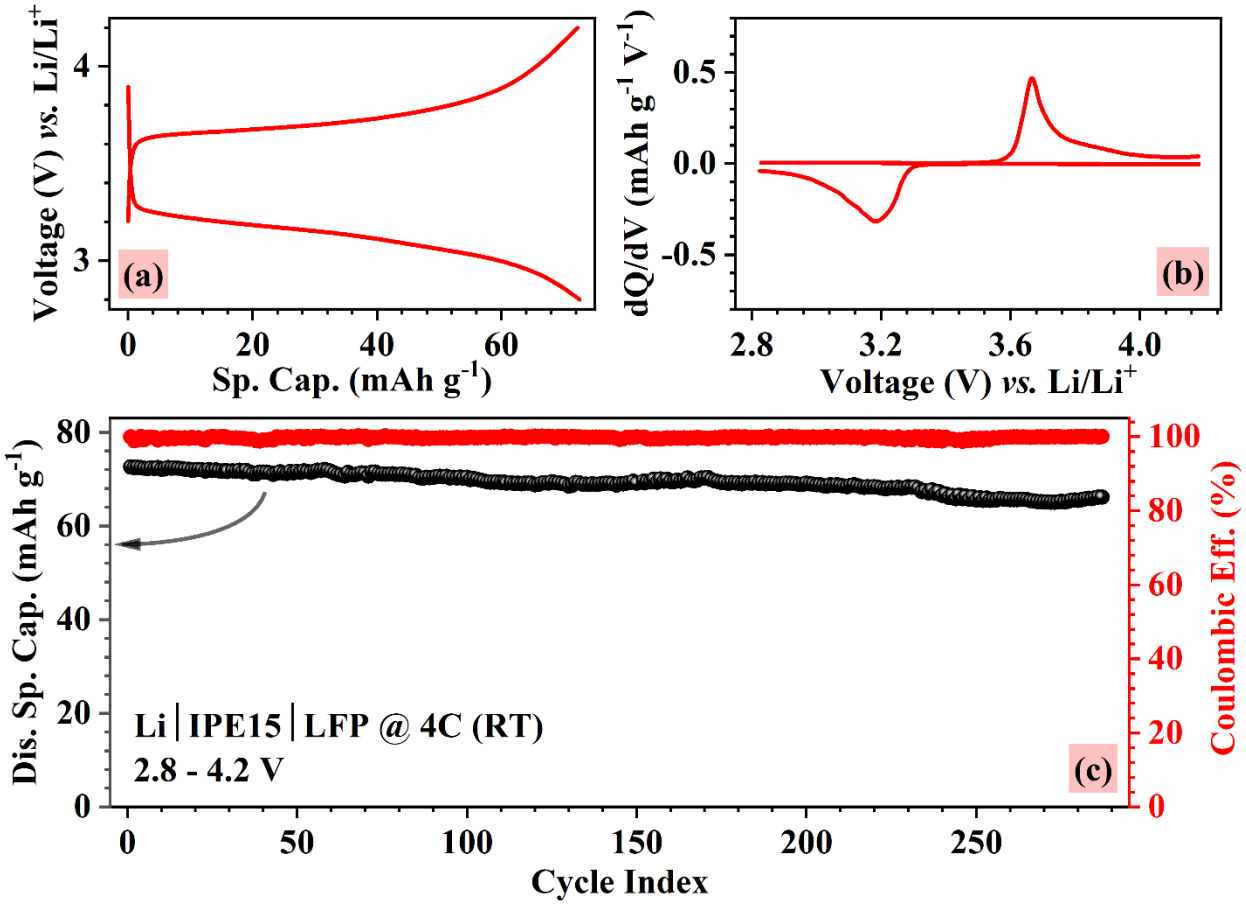

Fig. S17. Room temperature electrochemical performance of the Li|IPE15|LFP cell with an upper cut-off voltage of 4.2 V. (a) charge/discharge curve at 4C, (b) corresponding dQ/dV vs. V plot, and (c) cycling stability.

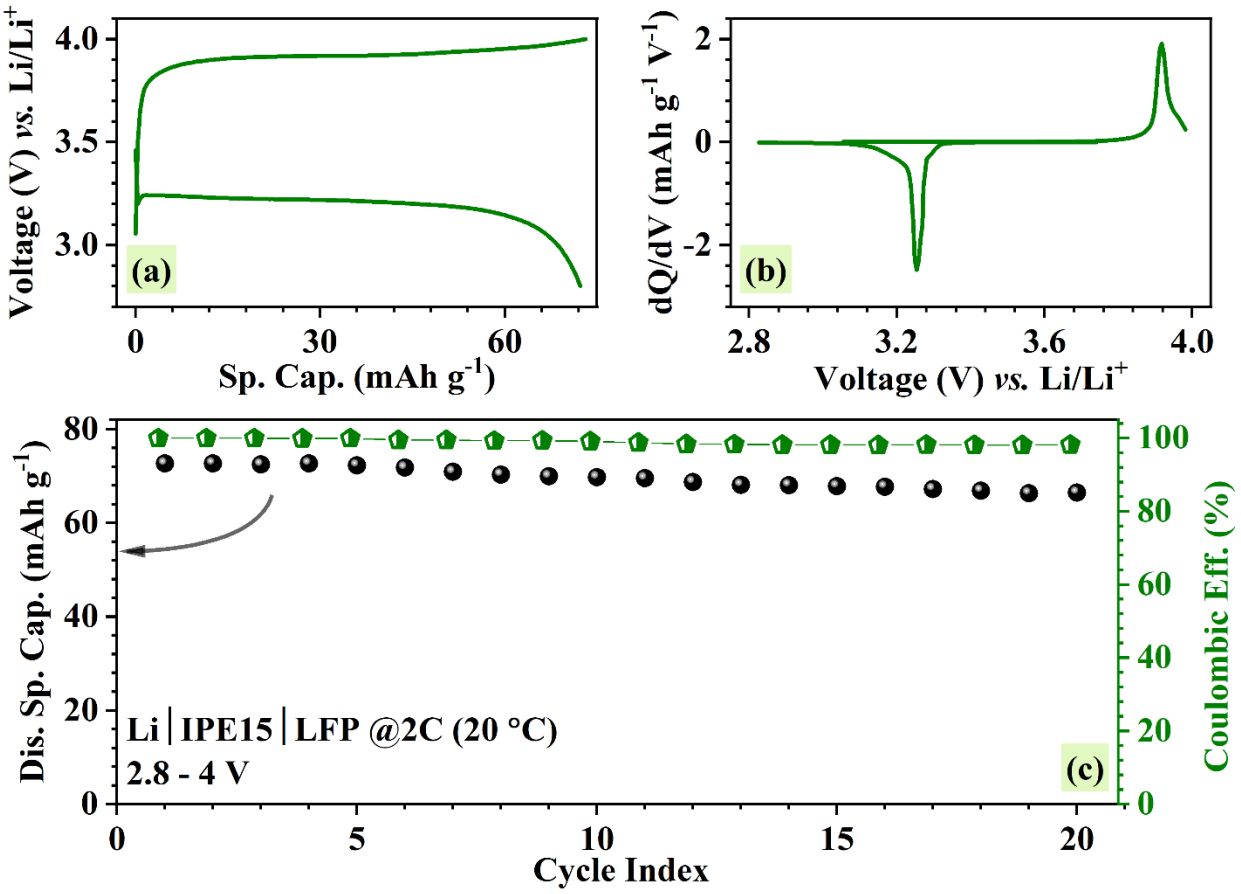

Fig. S18. Electrochemical performance of the cell at 20 °C with upper cut-off voltage 4 V. (a) charge/discharge curve of the Li|IPE15|LFP cell, (b) dQ/dV plot, and (c) cycling stability of the Li||LFP cell at 2C.

Table S1: FTIR spectral changes of IPE15 electrolyte before and after LSV scanning.

Spectral region (cm^{-1})	**Observation after LSV**	**Assignment**	**Scientific interpretation**	**Ref.**
772 → 777	Peak shifts to higher wavenumber	S-N-S bending / CF_3 deformation of $TFSI^-$	Change in Li^+-$TFSI^-$ coordination environment under high-voltage polarization	[3]
544-580	Peak splitting	SO_2 bending modes of $TFSI^-$	Conformational rearrangement of $TFSI^-$ anions due to altered ion-polymer interactions	[4]
706-756	Peak splitting	CF_3 bending / S-N stretching of $TFSI^-$	Local coordination heterogeneity without structural breakdown of the anion	[5, 6]
1036-1091	Peak splitting	SO_2 asymmetric stretching of $TFSI^-$	Altered dipole interactions under anodic polarization	[4]
1745-1825	New peaks appear (absent in fresh electrolyte)	Carbonyl-like vibrations / interfacial oxidation species	Formation of electrochemically induced interfacial oxidation products at high voltage; no evidence of cleavage of the $TFSI^-$ anion framework	[7]

References:

[1] P. Gami, A.K. Das, H.N. Vasavan, S. Saxena, N. Dagar, S. Kumar, PVDF-HFP/PVP-based miscible blend electrolyte for fast-charging lithium metal batteries, Electrochim Acta, 536 (2025) 146840. https://doi.org/10.1016/j.electacta.2025.146840

[2] P. Gami, M. Badole, H.N. Vasavan, A.K. Das, S. Saxena, N. Dagar, V. Srihari, S. Kumar, NASICON-type medium entropy $Li_{1.5}Sn_{1.0}Al_{0.5}Zr_{0.5}(PO_4)_3$ electrolyte for solid state Li metal batteries, J Power Sources, 618 (2024) 235214. https://doi.org/10.1016/j.jpowsour.2024.235214

[3] Y.-Q. Wang, H. Xu, B. Cao, J. Ma, Z.-W. Yu, In Situ Species Analysis of a Lithium-Ion Battery Electrolyte Containing LiTFSI and Propylene Carbonate, The Journal of Physical Chemistry Letters, 15 (2024) 5047-5055. https://doi.org/10.1021/acs.jpclett.4c00641

[4] K. Kim, L. Kuhn, I.V. Alabugin, D.T. Hallinan, Lithium Salt Dissociation in Diblock Copolymer Electrolyte Using Fourier Transform Infrared Spectroscopy, Frontiers in Energy Research, Volume 8 - 2020 (2020) https://doi.org/10.3389/fenrg.2020.569442

[5] I. Rey, J.C. Lassègues, J. Grondin, L. Servant, Infrared and Raman study of the PEO-LiTFSI polymer electrolyte, Electrochimica Acta, 43 (1998) 1505-1510. https://doi.org/10.1016/S0013-4686(97)10092-5

[6] A. Bakker, S. Gejji, J. Lindgren, K. Hermansson, M.M. Probst, Contact ion pair formation and ether oxygen coordination in the polymer electrolytes M[N(CF3SO2)2]2PEOn for M = Mg, Ca, Sr and Ba, Polymer, 36 (1995) 4371-4378. https://doi.org/10.1016/0032-3861(95)96841-U

[7] S.J. Wen, T.J. Richardson, D.I. Ghantous, K.A. Striebel, P.N. Ross, E.J. Cairns, FTIR characterization of PEO + LiN(CF3SO2)2 electrolytes, J Electroanal Chem, 408 (1996) 113-118. https://doi.org/10.1016/0022-0728(96)04536-6